The Life Cycle of a Thunderstorm in Three Dimensions

ROBERT WILHELMSON

Laboratory for Atmospheric Research and Center for Advanced Computations, University of Illinois, Urbana 61801

(Manuscript received 19 February 1974)

ABSTRACT

The results of an isolated three-dimensional thunderstorm simulation are reported. An initial wind shear of 1.54 m sec^{-1} km^{-1} is specified in the x direction and symmetry is assumed in the y direction about the central x-z plane. An erect cloud develops from an initial 3.7 km radius impulse as the updraft core is fed from all directions by moist and warm low-level air. After some time rain begins to fall and a downdraft developes downshear of the updraft core cutting off the major low-level supply of warm and moist air. Subsequently, the updraft core begins to tilt downshear and the center of the lower part of the updraft core is shifted away from the central x-z plane.

At middle cloud levels wind features reminiscent of flow about a cylinder are present. Both the hydrostatic and dynamic pressure appear to be important in decelerating flow upwind of the cloud.

Comparison with a similar two-dimensional simulation indicates that the three-dimensional cloud develops faster, grows taller, lasts longer, and travels farther and faster. This is indicative of differences in geometry which in turn are related to low-level moisture supply for cloud growth and to subsidence in the cloud environment.

1. Introduction

In the past few years the numerical simulation of individual thunderstorms cells in three-dimensional, sheared environments has been realized. These simulations have been prompted by flow restrictions in two dimensions that are often not found in nature. It has been shown by Ogura (1963), Murray (1970) and Soong and Ogura (1973) that the compensating downdraft in some non-sheared cloud environments is much weaker in an axisymmetric model than in a slab-symmetric model. This, in turn, may affect the storm duration and its propagational features. Fankhauser (1971) and Jessup (1972) have reported both horizontal diversion of chaff around the main updraft core of two different severe storms at about the 500-mb level and loss of chaff inside the core region. The dynamic pressure forces associated with the diversion of and speeding up of air around the sides of the storm may be important in understanding storm propagation and growth as pointed out by Newton (1967). Also, it is well known that the variation of wind direction with height is an important factor under proper thermodynamic and moisture conditions in both the generation of unstable conditions suitable for growth of mid-latitude severe storms and in their subsequent propagation, growth and lifetime.

The three-dimensional simulation of storms embedded in a sheared environment has been preceded and accompanied by two-dimensional slab-symmetric simulations. Recently reported simulations in two dimensions include those of Takeda (1971), Schlesinger (1973) and Hane (1973). After studying the effects of different horizontal environmental wind profiles on cloud life cycles each has also mentioned or implied that three-dimensional features may be important both qualitatively and quantitatively on their results. In either two or three dimensions questions of interest include dynamical details of storms; storm duration and intensity; storm propagation; location and amount of precipitation; net mass, momentum and heat transfers during a storm's lifetime; and, more generally, the important environmental and cloud parameters that determine the answers to these questions.

Steiner (1973) has recently reported three-dimensional simulations of dry and moist shallow convection. His model includes no precipitation and in one experiment a one-directional wind shear. Results reported include effects of varying the diffusion coefficient for dry convection, of varying the initial cloud impulse in moist convection, and of introducing a linear shear in the cloud environment, with attention focused only on the development stage.

The work reported here is another initial look at the importance of using a three-dimensional model, but for precipitating deep convection in an environment sheared in one direction. A three-dimensional simulation was made to investigate the first two points in the opening paragraph and to look into some of the questions of interest previously mentioned.

2. The cloud model equations

a. The equations of motion

The equations of motion in Cartesian coordinates and vector form are

$$\frac{\partial \mathbf{v}}{\partial t} = -(\mathbf{v} \cdot \nabla)\mathbf{v} - C_p \bar{\theta} \nabla \pi'$$
$$+ kg\left(\frac{\theta'}{\bar{\theta}} + 0.61 Q_v' - Q_c - Q_r\right) + \mathbf{F}, \quad (1)$$

where ∇ is the three-dimensional del operation, $\mathbf{v}$ the three-dimensional velocity vector, C_p the specific heat of dry air at constant pressure, θ the potential temperature, g gravity, Q_v the mixing ratio of water vapor, Q_c the mixing ratio of cloud droplets, and Q_r the mixing ratio of rainwater; $\pi = (p/P)^\kappa$ the nondimensional pressure, where p is the dimensional pressure, P the reference pressure taken to 1000 mb, $\kappa = R/c_p$, and R the gas constant for dry air; and $\mathbf{F}$ the turbulent diffusion vector. The overbar denotes base state or initial values. Comments and explanations can be found in Wilhelmson and Ogura (1972), with $\mathbf{F}$ modeled after Deardorff (1970). Since ambient wind is included here and significant modification of this wind by diffusion is not desired, only the deviation (u') from the initial ambient wind $(\bar{u})$ is used in computing $\mathbf{F}$. However, the diffusion coefficient values K are related to the total rate of dissipation of turbulent energy (Deardorff, 1972).

The diagnostic pressure equation can be formed from (1) by multiplying by the base state density $\bar{\rho}$ and taking the divergence, yielding

$$C_p \nabla \cdot (\overline{\rho \theta} \nabla \pi') = -\nabla \cdot [\bar{\rho}(\mathbf{v} \cdot \nabla)\mathbf{v} - \bar{\rho}\mathbf{F}]$$
$$+ \frac{\partial}{\partial z}\left[\bar{\rho}\left(\frac{\theta'}{\bar{\theta}} + 0.61 Q_v' - Q_c - Q_r\right)\right] - \frac{\partial}{\partial t}[\nabla \cdot (\bar{\rho}\mathbf{v})]. \quad (2)$$

The last term is zero provided the mass continuity equation

$$\nabla \cdot (\bar{\rho}\mathbf{v}) = 0 \quad (3)$$

applies throughout the domain.

b. Temperature and water equations

The thermodynamic equation for potential temperature is

$$\frac{\partial \theta}{\partial t} = -\mathbf{v} \cdot \nabla \theta + \frac{L}{C_p \bar{\pi}}(P2 - P3 - P4) + \nabla \cdot (K \nabla \theta'), \quad (4)$$

where $P2$ is the rate of condensation, $P3$ the rate of evaporation of cloud droplets, $P4$ the rate of evaporation of raindrops, and K the same eddy diffusion coefficient used in $\mathbf{F}$. The larger coefficient used by

Wilhelmson and Ogura (1972) was not found to be necessary to avoid the excessive small-scale temperature fluctuations noted by Deardorff (1972), this reflecting different properties of the numerical schemes employed.

The continuity equations for water vapor, cloud droplets and raindrops are, respectively,

$$\frac{\partial Q_v}{\partial t} = \mathbf{v} \cdot \nabla Q_v - P2 + P3 + P4 + \nabla \cdot (K \nabla Q_v'), \quad (5)$$

$$\frac{\partial Q_c}{\partial t} = \mathbf{v} \cdot \nabla Q_c - k_1(Q_c - a) - k_2 Q_c Q_r^{0.875}$$
$$+ P2 - P3 + \nabla \cdot (K \nabla Q_c), \quad (6)$$

$$\frac{\partial Q_r}{\partial t} = \mathbf{v} \cdot \nabla Q_r + \frac{1}{\bar{\rho}}\frac{\partial}{\partial z}(\bar{\rho} V_r Q_r)$$
$$+ k_1(Q_c - a) + k_2 Q_c Q_r^{0.875} - P4, \quad (7)$$

where V_r is terminal velocity of raindrops, given by Soong and Ogura (1973) as

$$V_r = 3634 (\bar{\rho} Q_r)^{0.1364}.$$

The autoconversion parameters k_1 and a, and the collection parameter k_2, are chosen to be the same as those used in Soong and Ogura, namely, $k_1 = 0$ for $Q_c \leqslant a$, $k_1 = 10^{-3}$ sec^{-1} for $Q_c > a$, $a = 10^{-3}$ gm gm^{-1} and $k_2 = 2.2$. The details of the determination of $P2$, $P3$ and $P4$ are also found in this paper.

c. Boundary conditions

For this study periodic boundary conditions have been chosen in both the x and y directions. Results implied by this regularity should be reasonable as long as the cloud lateral extent is small compared to the lateral extent of the domain and the lifetime of the cloud is not long.

The top and bottom boundaries are rigid and turbulent free with the free-slip condition permitting strong surface winds, i.e.,

$$w = 0, \quad \frac{\partial u}{\partial z} = \frac{\partial v}{\partial z} = 0. \quad (8)$$

The potential temperature and water variables are not located on these boundaries and are computed just inside the boundaries using (4), (5), (6) and (7). The advective scheme used requires no computational values for these variables. However, in calculating the diffusion terms and for other purposes the following top and bottom computational boundary conditions are used:

$$\frac{\partial}{\partial z}(\bar{\theta}, \theta', \bar{Q}_v, Q_v', Q_c, Q_r, K) = 0. \quad (9)$$

The upper and lower boundary conditions for the pressure equation follow from the above conditions and (1) and are

$$\frac{\partial \pi'}{\partial z} = -g\left(\frac{\theta}{\bar{\theta}}+0.61Q_v'-Q_c-Q_r\right)\Big/ C_p\bar{\theta}, \quad (10)$$

where $\mathbf{k}\cdot\mathbf{F}$ is considered zero on these boundaries.

d. Initial conditions

The initial environmental conditions are used to specify the base state. The base state temperature $\bar{T}$ ranges from 25C at $z=0$ down to about -56C at $z=15$ km, decreasing with height at rates of 9.8, 6.0 and 4.0C km^{-1} in layers of 0–1.2, 1.2–8.4 and 8.4–15 km, respectively. This temperature profile is conditionally unstable below about 5 km. The base state relative humidity ranges from 80% at $z=0$ to 98% at $z=1.2$ km, then linearly decreases to 30% at 10.2 km and finally is maintained at 30% to 15 km. This provides a considerable moisture supply near the ground. Using these values $\bar{p}$, $\bar{\pi}$, $\bar{\theta}$ and $\bar{\rho}$ are calculated using the hydrostatic equation, the equation of state, and $\bar{T}=\bar{\pi}\bar{\theta}$ [as in Wilhelmson and Ogura (1972)]. While these conditions are not taken from some real sounding, they nevertheless permit a study of some basic storm dynamics.

An initial axisymmetric impulse or cloud is horizontally centered in the domain from $z=0.9$ to 2.1 km using the formula

$$\theta = \bar{\theta}+A\left(2-\frac{z}{1.5}\right)\left(\frac{z}{1.5}\right)\cos\left[\frac{\pi}{2}\left(\frac{r}{r_m}\right)\right],$$

where $A=0.3$C is the maximum increase occurring at the domain center and $z=1.5$ km, $r_m=3.7$ km is the cloud radius, and $0 \leqslant r \leqslant 3.7$ km. The relative humidity is assumed to be 100% at all θ-modified locations. No cloud water is initially specified.

The initial wind profile varies linearly in the x direction from -6 to 6 m sec^{-1} between 0.3 and 8.1 km and is constant above and below these levels. This gives a moderate positive shear of about 1.5 m sec^{-1} km^{-1}. The profile used is considered sufficient for present purposes, although no particular storm profile is being modeled and the environmental wind does not change direction with height as frequently observed for severe storms in mid-latitudes.

The initializations for the two-dimensional case and the central x-z plane of the three-dimensional case (defined in the next section) are the same.

3. Numerical considerations

a. Numerical techniques employed

All time derivatives are approximated with first-order, forward time differences. The forward time difference is used to help minimize auxiliary storage requirements and shuffling of data between main and auxiliary storage. This reduces both running time and cost in comparison to the use of higher order time differences. Pressure and diffusion terms are calculated using centered differences. Velocity advective terms are calculated using upstream space differencing despite the damping characteristics of such differencing, as detailed effects of turbulence are not of primary interest in this study. The remaining advective terms are calculated by a modified upstream scheme given by Soong and Ogura (1973).

This latter scheme is based on the flux form of these advective terms and, with forward time differencing, linearly conserves advected θ, Q_v, Q_c and Q_r in a closed domain. The partial advection of Q_r due to its weight as given by the second term on the right of (7) is included, provided that no Q_r reaches the ground. The modified scheme also has the advantage that Q_c and Q_r do not become negative, eliminating any need to adjust the Q_c and Q_r fields to remove any negative water that often can result from truncation errors in their advection. If water changes from one category to another or falls out, the total water content including the fallen rain is conserved. Further, using centered space differences for the diffusion terms and the z boundary conditions indicated previously, total water conservation is retained. It should be noted that in the above calculations the amount of rainfall from time $t-\Delta t$ to t is computed from the rainfall rate at the ground at the time $t-\Delta t$ multiplied by Δt, where $Q_r(x,0,t) = Q_r(x,\Delta z/2,t)$.

Another cost saving technique is to choose a new Δt at frequent intervals on the basis of a numerical stability criterion. The von Neumann criterion is derived separately for the three-dimensional linear advection and diffusion equations are combined such that the necessary condition for stability is assumed to be

$$\Delta t \leqslant 0.9\left[\left(\frac{\Delta}{u+v+w}\right)_{\min}\left(\frac{\Delta^2}{8K}\right)_{\min}\right]_{\min}, \quad (11)$$

where $\Delta=\Delta x=\Delta y=\Delta z$ and the inner minima are taken over the whole domain. The factor 0.9 is considered as a safety factor used to preserve stability for the more general equations. It turns out that for the experiments reported here the advective requirement is the limiting one, typically by a factor of 10.

The largest Δt allowed is 30 sec and all others used are also evenly divisible into 60 sec. The initial linear wind profile was orientated with the advective criterion in mind, as the Δt choice depends partly on the absolute magnitude of u. In the present differential model the addition of a constant to the initial wind profile will not alter the results apart from a change in horizontal advection of the system as a
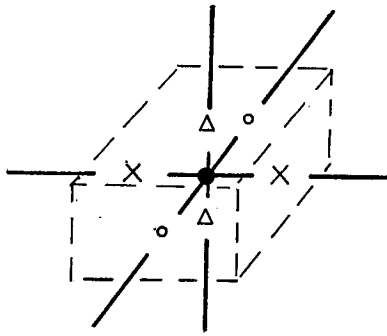
FIG. 1. The three-dimensional staggered grid arrangement (○: v, π, θ, Q_v, Q_c, Q_r; △: w; ×: u).

whole by the constant value. However, the numerical advective scheme used does not preserve this property. A two-dimensional simulation similar to the one reported in Section 5, but with the use of a constant of 6 m sec^{-1}, indicates this to be true. The maximum vertical velocity decreased by 1.2 m sec^{-1} and the cloud lifetime appears to be shortened 3–5 min by this change. However, the basic dynamical features remain similar.

The staggared grid arrangement given in Fig. 1 is used, where w values lie on the top and bottom boundary planes. This grid arrangement is convenient for expressing the finite difference form of the pressure equation (2) which is derived from the finite difference form of (1). A fast Fourier transform routine given by Williams (1969) is used in solving the pressure equation.

The grid interval used in all directions is 600 m. The dimensions of the domain are 38.4, 38.4 and 15 km in the x, y and z directions, respectively. Symmetry about the x-z plane at $y = 19.2$ km is permitted by the initial conditions and this reduces the typical 102,000 data points per field to 53,000 for the half domain (i.e., 64×33×25). The two-dimensional x-z plane located at $y = 19.2$ km is referred to as the central or central x-z plane.

It should be noted that $v = 0$ in the central plane and that the y advective terms in the u, v and w equations are thus zero since the upstream scheme is employed. However, the y advective terms in the potential temperature and water equations are not typically zero due to use of modified upstream differencing.

b. *Amplifying internal gravity waves and numerical instability*

In both the two- and three-dimensional simulations what appear to be amplifying internal gravity waves occur in the upper part of the domain as the clouds decay. These waves are particularly strong in two dimensions after 40 min and noticeable in three dimen-

sions at 55 min. Thus, no discussion of results beyond these times is made.

This amplification appears to be primarily due to the use of centered space differencing for the pressure derivatives coupled with forward time differencing for the velocity and potential temperature time derivatives. The advective criterion used in (11) does not apply to these waves as the advective terms are not responsible for their propagation. The von Neumann necessary condition for stability of the linearized gravity wave equations in a stable environment is not satisfied with resulting amplification for all wavenumbers (see Appendix). This might have been suspected as forward time, centered space differencing is also unstable for the wave solution of the simple one-dimensional advective equation. Further, this amplification for any given Δt will increase with increasing atmospheric stability. However, the von Neumann analysis indicates that the amplification over some given time period may be reduced by the choice of smaller Δt. Some test simulations using the two-dimensional cloud model indicate this to be true, but at the expense of increasing the implicit diffusion associated with the upstream advective differencing used.

c. *Remote computer access*

A portion of the work reported here was a successful effort to debug and run the three-dimensional code on the UCLA IBM 360/95, but from the University of Illinois. Remote access was accomplished through the ARPA communications network[1] having nodes at UCLA and the University of Illinois. This particular effort involved one of the first large codes to be run using the network and indicates some of the advances made in remote access during the past five years for handling large amounts of data.

Remote access permitted use of needed computer resources that were not available at the University of Illinois without leaving duties and interaction with colleagues at the University. Coupled with the three-dimensional coding was an effort to help in the development of graphical capabilities to display the data on any one of several display or hardcopy devices at the University of Illinois network node. Such graphic display is extremely helpful in looking at the large amount of data typically associated with three-dimensional simulations.

. [1] The ARPANET was initiated by the Advanced Research Projects Agency of the Department of Defense for the purpose of connecting via 50,000 bits sec^{-1} high-speed data transmission lines . a number of research centers and projects around the United States. The reliability of this store-and-forward message transmission network is estimated to be a one bit error going undetected per year. A developmental report has been written by Roberts and Wessler (1970) and experience using the network at the University of Illinois has been reported by Sher (1973).

4. Results of the three-dimensional simulation

a. A general description of the central plane

The maximum values for w, θ', Q_c and Q_r in the cloud region and also throughout the domain are given as a function of time in Fig. 2. The maximum vertical velocity increases rapidly from 10 to 24 min reaching 28 m sec^{-1}, this peak having been preceded by increases and peaks in Q_c and θ'. Such vertical velocities are not uncommon in severe storms as emphasized recently in a number of observational determinations of vertical motions in severe convective storms.[2] The heights at which these peak values occur are included in Fig. 2. The Q_r peak is a bit higher and about 6 min later than the w peak, while at the same time the maximum liquid water content $\bar{\rho}Q_r$ is about 1 km lower. There are secondary peaks for w and θ' occurring about 10–15 min after the first peaks. This appears to be at least partially the result of less liquid water drag in the maximum velocity area due to a relative shift of the maximum Q_r area to the right of the maximum velocity area. The results of the Q_c, Q_r parameterization are evident in that Q_c never exceeds 3 gm kg^{-1} while Q_r reaches above 12 gm kg^{-1}.

The motion is contrained by y symmetry about the central x-z plane, as previously mentioned. The central plane contours at 25, 35 and 45 min in Figs. 3–9 reveal the main central plane features in the model simulation. By 25 min the initial symmetric state has become noticeably distorted. The larger horizontal w, θ', Q_c and Q_r gradients along the upshear or left side of the cloud are indicative of cloud growth and movement to the left. The low-level inflow supplying moisture for cloud growth on the left comes from both sides of the cloud. The upper level outflow from the cloud, however, is primarily downshear. This is revealed in Fig. 3 by the magnitudes of u in the outflow centers, which when adjusted for cloud movement to the left further emphasize downshear outflow. This airflow pattern may account for the distant location of the upper right compensating downdraft and the rightward slant of the vertical velocity, moisture and water fields to the cloud right.

Environmental wind modification can also be associated with the airflow pattern. The shear at $x=5$ km has over the cloud depth been reduced, while the shear at $x=23$ km has been increased. Such modification, though, is not unique to initially sheared environments. One would expect a similar modification for a growing cloud in a two-dimensional slab-symmetric model without shear on the basis of horizontal inflow and outflow patterns about the cloud central
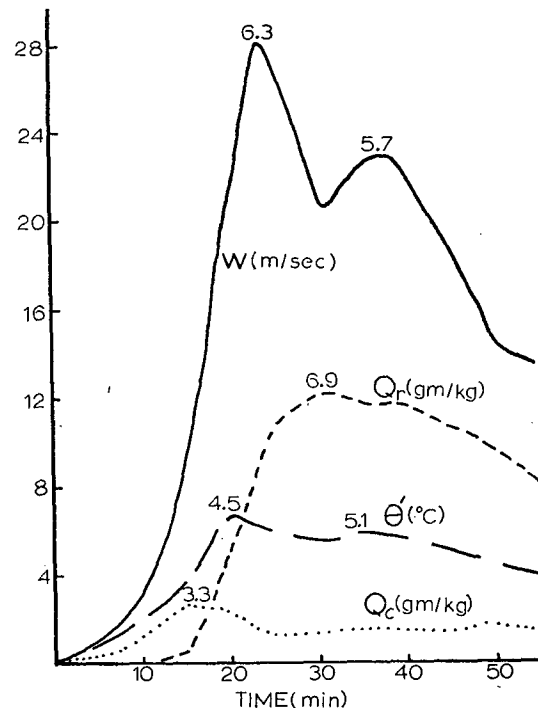

FIG. 2. The maximum w, θ', Q_c and Q_r curves with time. Heights (km) are indicated for peak values.

axis.[3] Such flow results in a reduced or negative shear to the cloud left and an increased or positive shear to the cloud right.

In Fig. 3 the contour lines of u in the cloud and below the maximum vertical velocity region are also notable. However, the extent to which the vertical transport of momentum is responsible for the lack of shear in this region is difficult to determine. Further, direct observational evidence for a lack of shear in this region for clouds developing in an environmental shear appears to be scarce. The work of Asai (1967) may indicate such a feature for cumulus updrafts observed by rawinsondes at Wajima, Japan.

The θ' contours at 25 min in Fig. 4 show the warming effect of subsidence, particularly at middle levels near the cloud boundary and below the maximum downdraft centers. Cool regions are located both below and to the lower right of the cloud, perhaps associated with air approaching the cloud from the right in the lower levels and rising without becoming saturated. Dry adiabatic cooling and evaporation has occurred in the upper cloud area. Also, it is notable that θ' is positive in the lower updraft core in light of recent reports of negatively buoyant updrafts in low levels of severe storms (e.g., Foote and Fankhauser, 1973).

The most noticeable pressure changes occur in the upper part of the cloud where a high develops in

[2] *Preprints Eighth Conf. Severe Local Storms,* 15–17 October 1973, Amer. Meteor. Soc.

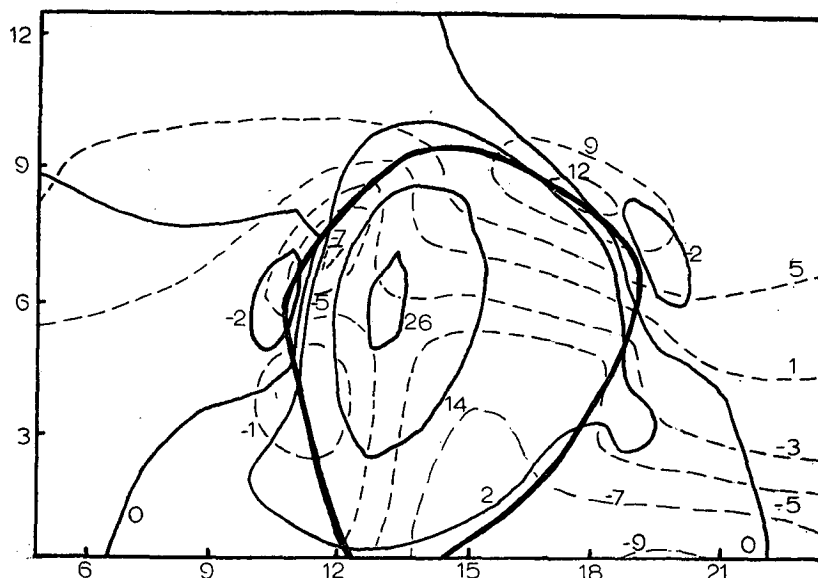[3] For example, see Wilhelmson and Ogura (1972), Fig. 2.

FIG. 3. Central plane contours for w (solid) and u (dashed) in m sec^{-1} at 25 min. The thick solid line encloses $Q_r \geqslant 1$ gm kg^{-1} both here and later. The lower boundary line is at a height of 0.3 km here and in all x-z contours. Also, only part of the full domain contours are shown.

this vertical plane. The pressure is the sum of the dynamic, buoyancy and drag pressure as defined in Wilhelmson and Ogura (1972). Therefore, an interpretation in relation to the velocity, temperature and water fields alone is difficult since in this region all should be important. In general, however, it can be said that the pressure force at this time opposes cloud

growth in all but the lowest levels and provides an outward acceleration force in the cloud top region.

The liquid water fields in Fig. 5 indicate that cloud water is typically converted to rainwater in the lower levels, i.e., where $Q_c > 1$ gm kg^{-1}, and then this rainwater is carried further aloft due to the large vertical velocities. The maximum rainfall intensity at 25 min
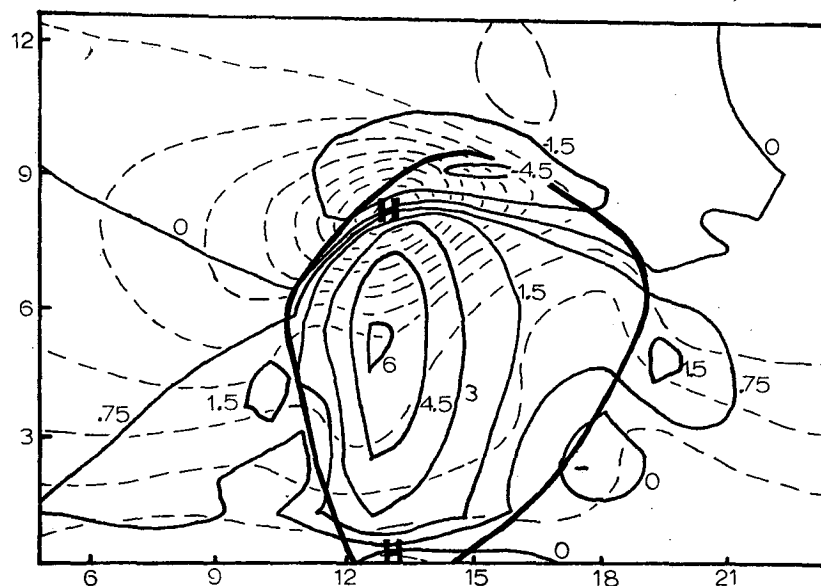

FIG. 4. Central plane contours for θ' (solid) in °K and π' (dashed) at 25 min. The π' contours are equally spaced and high (H) and low (L) π' centers are indicated. Here the lowest π' contour is just above the high at the ground.
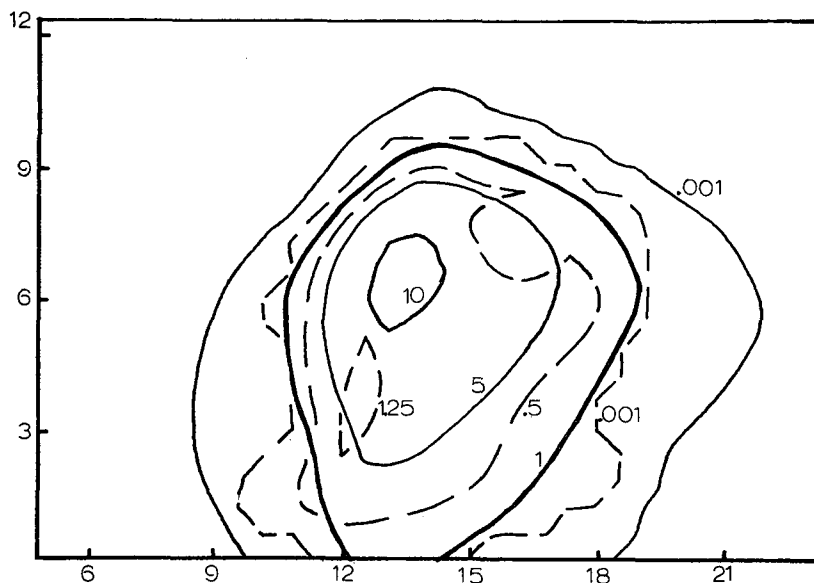
Fig. 5. Central plane contours for Q_c (dashed) and Q_r (solid) in gm kg^{-1} at 25 min.

is 38 mm hr^{-1} and is located below the w, θ' and Q_r maxima.

A quasi-steady-state dynamical configuration never occurs as a downdraft forms to the lower right of the cloud by 30 min. This appears to have resulted from the drag of precipitation on the air in this region and evaporation may also have had some effect. The increasing downdraft is evident at 35 min in Fig. 6. The original and primary warm and moist low-level air supply from the right is diverted around the cloud, resulting in a weakening of the updraft. Both the updraft and θ' contours in the cloud region begin to tilt to the right and become narrower as time passes. Gravity waves also become evident in the upper levels.

The downdraft continues to strengthen while the tilt in the updraft and θ' contours remain about the same as illustrated at 45 min in Figs. 7 and 8. The downdraft has spread over a large horizontal region and the maximum downdraft velocity, -5 m sec^{-1}, is about the strongest in the simulation. The downdraft covers almost all of the rain area.
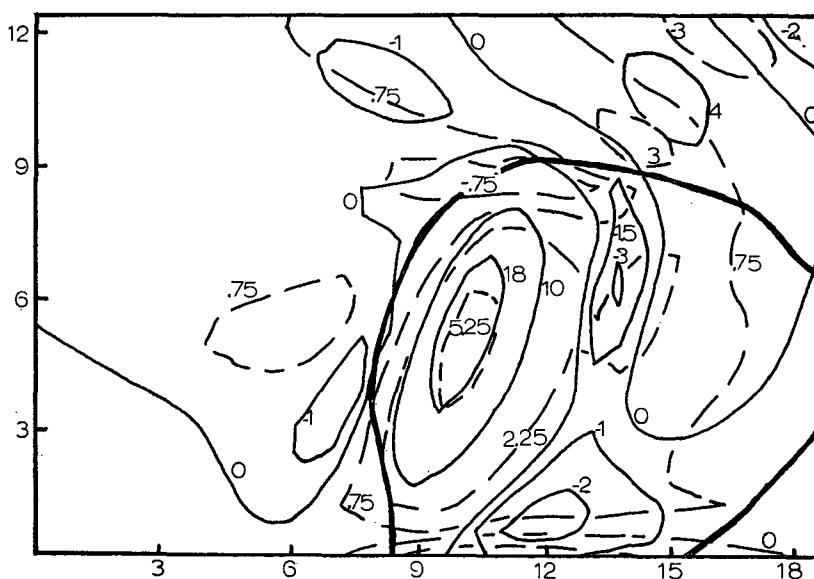

Fig. 6. Central plane contours for w (solid) in m sec^{-1} and θ' (dashed) in °K at 35 min.
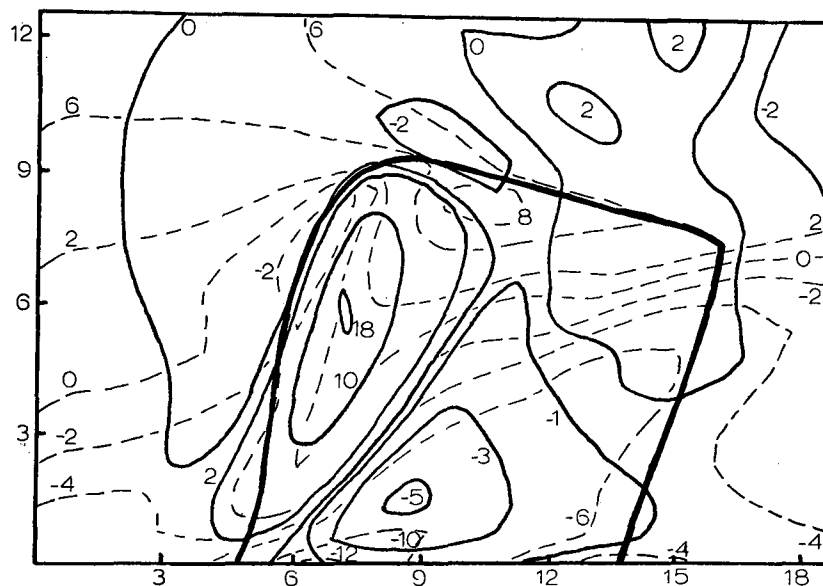Note shift in area displayed due to cloud movement.

FIG. 7. As in Fig. 3 except at 45 min.

The horizontal velocity is noticeably changed from that at 25 min, particularly in the lower region. There is a very strong u velocity below the updraft of -12 m sec^{-1}, 6 m sec^{-1} less than the original environmental value at this height. This is associated with the downdraft diverging as it reaches the ground. Above this and in the updraft core region the tilt of the u contours is similar, as at 25 min, to that of the updraft core. Thus, in contrast to 25 min the vertical gradients of u are now stronger in the core region below the maximum velocity. Also, the outflow region in the cloud top is weaker.

The pressure deviation contours in Fig. 8 indicate a pressure high in the cloud top region and both a pressure high and low in the lower levels. The lower high is below the maximum downdraft and to the right of the maximum cooling while the low is below the maximum updraft and heating and above the maximum cooling. Again, in general, the pressure force opposes cloud growth except in the lowest levels.

The Q_c field of cloud droplets, as seen in Fig. 9, is located primarily in the cloud updraft region. The small amount to the upper cloud right is probably a result of condensation due to the coupling of moisture
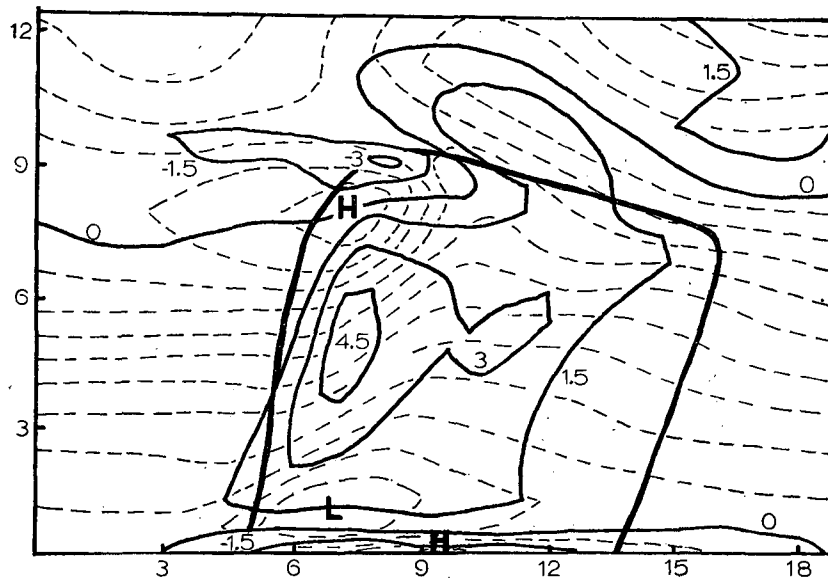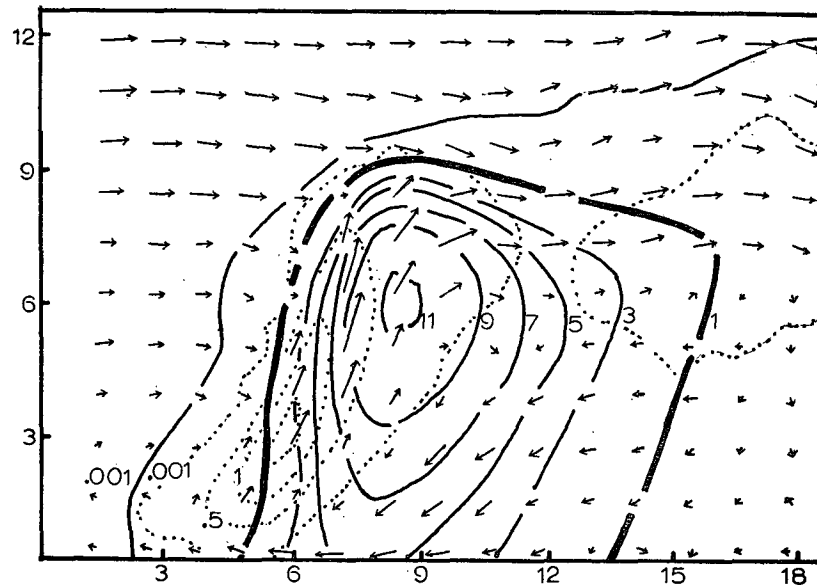

FIG. 8. As in Fig. 4 except at 45 min.

FIG. 9. Central plane contours for Q_c (dotted) and Q_r (solid) in gm kg^{-1} and relative wind vectors at 45 min. The magnitude of the largest vector is about 20 m sec^{-1}.

from evaporating cloud droplets and raindrops that are carried downshear and the apparent gravity wave updraft seen in Fig. 7. This cloudy region resembles an anvil in appearance but is not the direct result of droplet blowoff from the cloud top. There again is a considerable amount of rainwater to the cloud right, as at 25 min but not at all levels. This results from the advection of rainwater from the updraft core with the downshear outflow and its subsequent descent to the ground. The maximum rainfall intensity of the simulation, 157 mm hr^{-1}, occurs below the maximum Q_r value but several grid intervals (1.2 km) to the right of the maximum vertical velocity.

b. Cloud movement in the central plane

The air velocity vector profile taken relative to the cloud movement changes considerably from the growing to the decaying stage. From 25 to 35 min the general relative flow changes from that of a strong erect updraft fed by moist converging air in the lower levels to that of a strong but somewhat tilted updraft with a low-level downdraft to the right of it. At 45 min the flow pattern given in Fig. 9 indicates that the supply of moist air has been generally cut off, at least in this plane. At all these times there is little or no counterclockwise circulation upshear of the cloud while the clockwise circulation downshear is associated with falling out of rain. Strong horizontal components of wind are evident near the ground in the rain area at 45 min, with middle level air descending in the downdraft and some apparently passing under the cloud to the left.

The calculation of cloud speeds needed in order to determine relative air flow patterns is complicated by

the changing nature of the cloud. For this simulation the speed was determined by noting how fast the maximum w location moved in x, the maximum w always being associated with the original thunderstorm cell and always lying in the central plane. Following the maximum θ' gave similar speeds. The cloud speeds at 25, 35, 45 and 55 min are -4, -6, -3.5 and -3 m sec^{-1}, respectively. The height of the maximum w locations remains close to 6 km at all these times and together with the observation that the updraft core still extends down to the lower kilometer during this 30-min time span indicates a continued arrival of new parcels at this level. However, the non-relative horizontal velocity of these parcels reaching the maximum vertical velocity location has changed from about -3 m sec^{-1} at 25 min to 0 m sec^{-1} at 35 min and then less rapidly to 1 m sec^{-1} at 45 min. An explanation of these changes in cloud speed and parcel speed is not attempted here except to say that it is plausible to consider these changes to be related to the formation of a downdraft and to subsequent changes in parcel origin near the ground and also to changes in the profile of the updraft core.

The cloud speeds determined vary over the speeds of the initial environmental wind in the lower 2 km. Keeping this in mind it is interesting to note the steady-state relative updraft profiles in Newton (1966). There is an upshear tilt to those profiles in Fig. 6 of this paper. These were computed given, as in this study, a linear environmental wind profile, but assuming the cloud is moving with the environmental wind at a higher (4 km) level. The higher this level is the greater the upshear incline for a given updraft profile. A distinct upshear tilt at any time or level
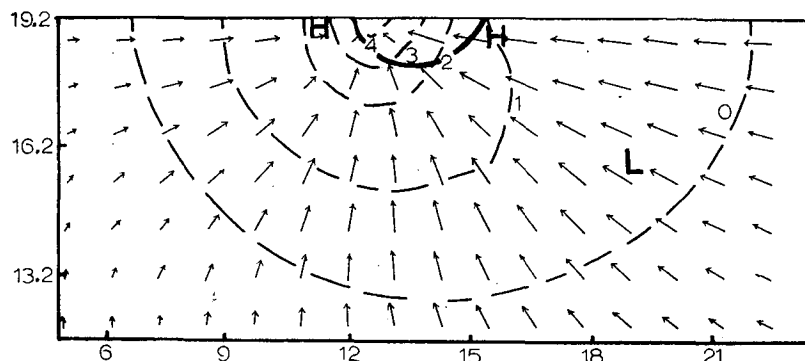
FIG. 10. Horizontal plane contours for w (dashed) in m sec^{-1} and relative wind vectors at 0.9 km and 25 min. The 1 gm kg^{-1} Q_r contour (thick solid) and π' relative highs (H) and lows (L) are included. The magnitude of the largest vector is 4.7 m sec^{-1}.

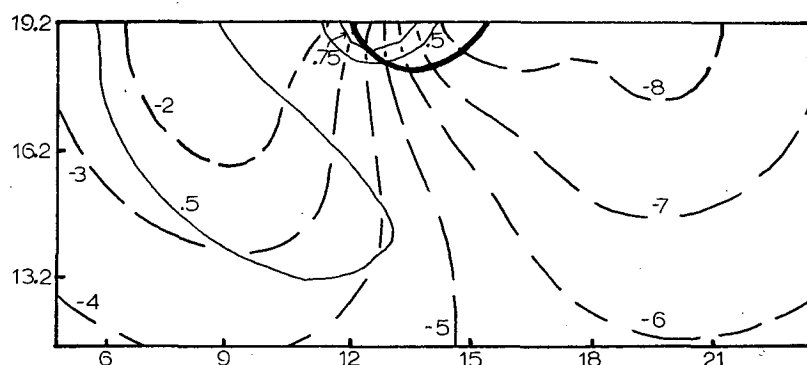FIG. 11. Horizontal plane contours for θ' (solid) in °K and u (dashed) in m sec^{-1} at 0.9 km and 25 min.

is not, however, evident for the profile simulated here. This appears to be associated with the non-steady-state nature of the simulated cloud and with a cloud speed that is similar to the low-level environmental wind if Newton's formula is considered. Newton's formula could also account for the downshear tilting of the updraft core between 25 and 35 min in that the maximum vertical velocity has been reduced and the updraft speed profile changed accordingly. Further, the lack of tilting between 35 and 45 min may be related to smaller changes in the maximum vertical velocity and updraft speed profile (see Figs. 2, 3, 6 and 7).

c. A horizontal view

The motion in the central x-z plane gives only a partial perspective on the cloud development, even though y symmetry is employed. Figs. 10–22 show basic features at the 0.9-, 3.9- and 6.9-km levels at 25 and 45 min. At 25 min in Fig. 10 the relative horizontal flow at 0.9 km converges from all directions to the center of the updraft core. In light of the discussion in the last section this would be true unless the cloud speed was greater than -2 m sec^{-1}. The stronger winds come from the right, that is, from the

direction of the initially specified environmental wind at this level. The updraft region has increased in size during the development stage as its core moves to the left. There is not much increase of potential temperature in the updraft core of Fig. 11 due to condensation, as originally this level was almost saturated. Noticeable also in the θ' field is the slant downward and to the right of the leftmost contour line. This slant is indicative of the cloud proceeding left along the central plane faster than along its y outskirts, particularly at lower levels. The water fields indicate that Q_r area trails behind that of Q_c. This is due to rain from above. The smallness of Q_c indicates this level to be about that of the cloud base.

The relative wind field at 3.9 km and 25 min in Fig. 12 reveals air flow both into and around the cloud region.[4] In the updraft at this level the air is moving counterclockwise, particularly to the right of the updraft center. Again, this would also be true unless the cloud speed was greater than -2 m sec^{-1}. At this time there is still a considerable but decreasing region of updraft outside the $Q_r = 1$ gm kg^{-1} contour. There

---

[4] Care should be taken in reading these horizontal vector patterns as the magnitude of the largest vector may vary from one figure to another.
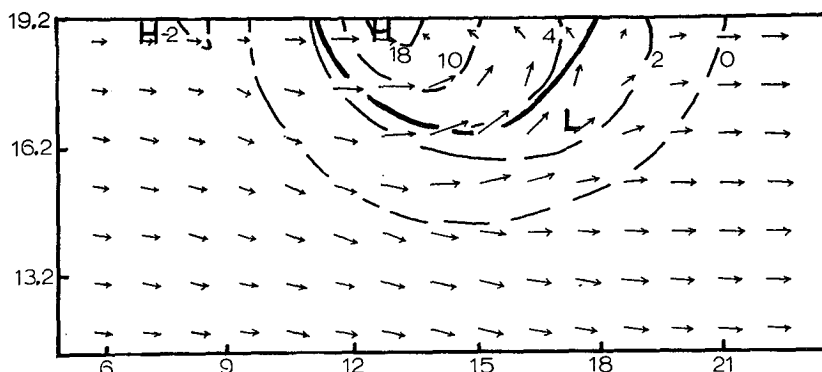
FIG. 12. As in Fig. 10 except at 3.9 km and 25 min. The magnitude of the largest vector is 7.5 m sec^{-1}.

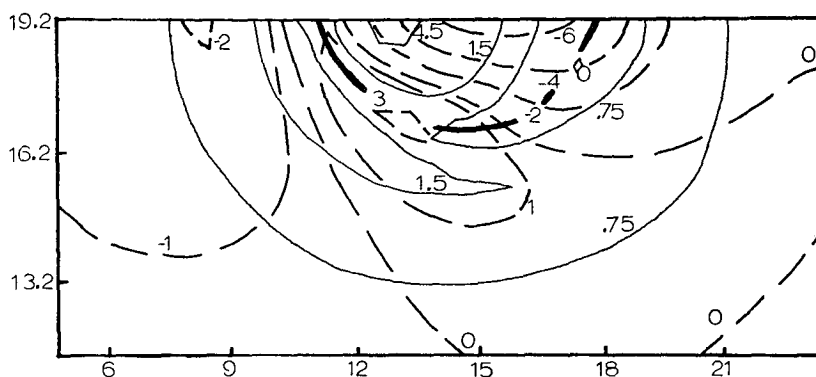
FIG. 13. As in Fig. 11 except at 3.9 km and 25 min.
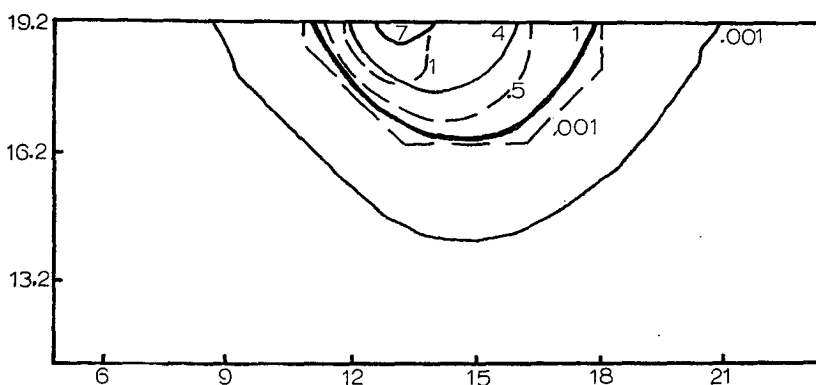

FIG. 14. Horizontal plane contours for Q_c (dashed) and Q_r (solid) in gm kg^{-1} at 3.9 km and 25 min.

are also noticeable positive u velocity centers at this (Fig. 13) and later times located to the side and along the $Q_r = 1$ gm kg^{-1} contours. The initial environmental wind at this level was -1.38 m sec^{-1} indicating 3–4 m sec^{-1} changes at these centers. Accompanying this motion are larger gradients in w, θ', Q_v', Q_c and Q_r on the cloud left as seen in Figs. 12–14 and as previously mentioned in the central plane discussion.

The maximum updraft occurs at or below 6.3 km at all times. Just above this level at 6.9 km and at 25 min (Fig. 15) and thereafter, the relative air flow is around and out from the core toward the right. The updraft region is smaller than at lower levels. The negative θ' values to the cloud left in Fig. 16 are indicative of previous dry adiabatic lifting and evaporation in this region.
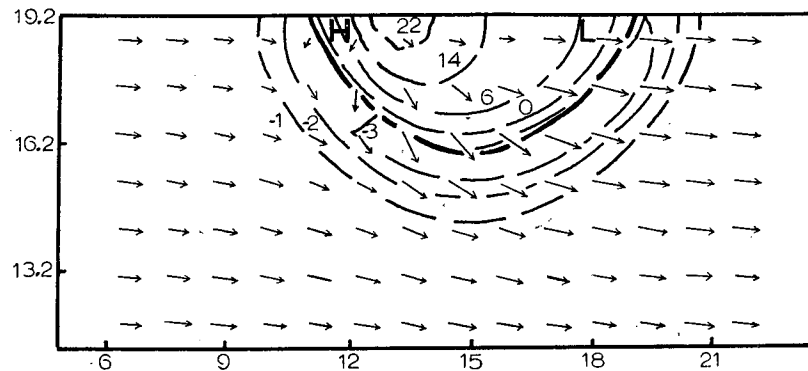
FIG. 15. As in Fig. 10 except at 6.9 km and 25 min. The magnitude of the largest vector is 13.2 m sec^{-1}.

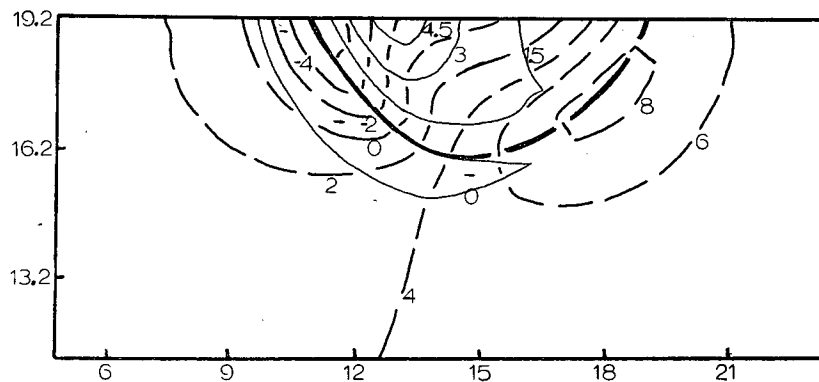

FIG. 16. As in Fig. 11 except at 6.9 km and 25 min.

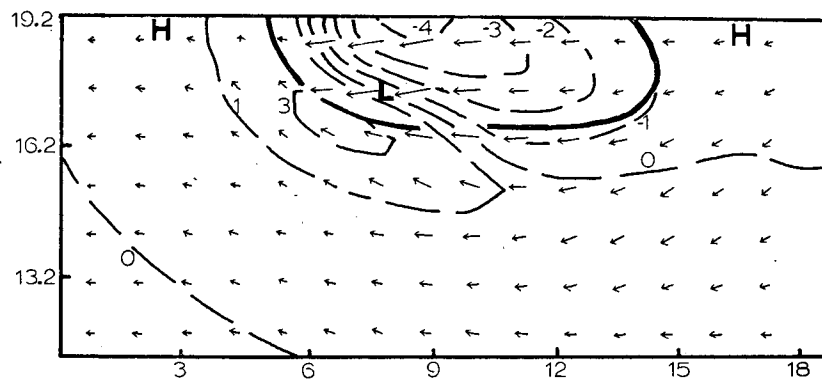FIG. 17. As in Fig. 10 except at 0.9 km and 45 min. The magnitude of the largest vector is 8.2 m sec^{-1}.

At 45 min and $z=0.9$ km in Fig. 17 the strongest part of updraft is located away from the center plane. This relocation is correlated with a θ' increase in the same region as seen in Fig. 18. The reason for the change of location probably includes the effects of downdraft outflow together with the moist air being supplied from downshear by air passing around the rain region as it moves relatively upshear. The maxi-

mum downdraft remains in the central plane as the largest amount of precipitation remains in this plane. There is little condensation or cloud droplets at this level in the updraft indicating that it is probably just above cloud base.

At $z=3.9$ km in Fig. 19 it is seen that the updraft core is located over the downdraft at 0.9 km and its maximum is again in the central plane. The w and
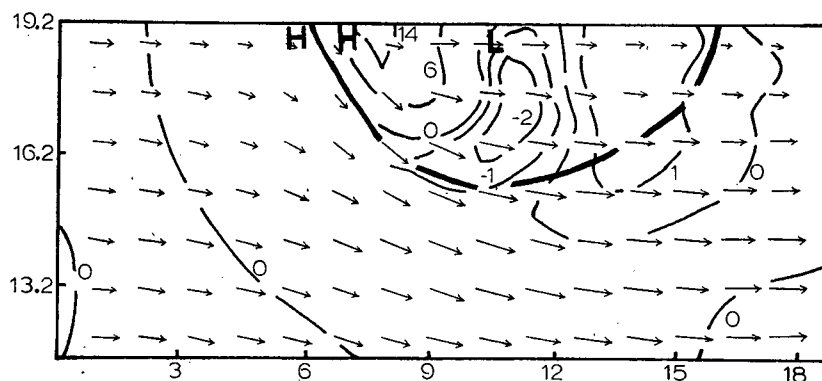
FIG. 18. As in Fig. 11 except at 0.9 km and 45 min.

FIG. 19. As in Fig. 10 except at 3.9 km and 45 min. The magnitude of the largest vector is 7.0 m sec^{-1}.

FIG. 20. As in Fig. 11 except at 3.9 km and 45 min.

vector fields indicate air entering and passing around the updraft from the left with some of this air entering the right downdraft. Again, there is a noticeable increase in u along the side of the $Q_r=1$ gm kg^{-1} contour in Fig. 20.

At 6.9 km air is diverging to the right from the updraft (Fig. 21). The updraft core region is about the same size as at 3.9 km but also to the right. The maximum w occurs about 1 km below at 5.7 km.

The θ' and u contours in Fig. 22 are included for completeness.

d. Pressure

Newton and Newton (1959) presented a general schematic cloud model in shear in which the induced dynamic pressure deviations were considered similar to those induced by fluid flow around a cylindrical

FIG. 21. As in Fig. 10 except at 6.9 km and 45 min. The magnitude of the largest vector is 10.0 m sec^{-1}.

obstacle. More recently, Fankhauser (1971) has used aircraft wind and radar chaff trajectories to show that a thunderstorm may act as an obstacle to airflow at mid-tropospheric heights in a manner similar to solid obstacles in relative streaming flow. This implies a decrease in velocity upwind of the obstacle or cloud, coupled with increased velocities around the sides. He also noted that internal cloud circulations were not entirely insulated from environment flow as some chaff elements were lost as they crossed the radar echo boundary. Jessup (1972) used a more densely distributed series of chaff at mid-levels to study air motion for another Great Plains thunderstorm. He concluded that of nine chaff bundles which were released upwind of the storm and entered the radar echo region, three appeared to move through the precipitation region and emerge downwind of the storm while the six nearest the hook echo did not reappear. Further, using the trajectories of four of these six bundles near the hook echo he determined a speed minimum upwind of the hook echo and increased speeds along the sides, again indicative of obstacle flow.

Illustrations of wind features reminiscent of flow about a cylinder at mid-levels occur at 3.9 km at 25 and 45 min in Figs. 12, 13, 19 and 20. At both times a low u center is located on the central axis and upshear of the cloud and a high u center to the side as mentioned in the previous section. Although no parcel trajectories have been determined it would appear from the relative vector patterns that some upshear air enters the core region and some is diverted around it.

The nondimensional pressure associated with this flow pattern changes from 25 to 45 min. At 25 min the relative horizontal high is located near the center of the updraft core and is probably more closely associated with excess hydrostatic or buoyancy pressure than with dynamic pressure. This pressure results from the buoyancy terms on the right-hand side of (2). Barnes (1970) indicates that increased hydrostatic pressure at mid-levels in the core of an updraft is an important factor in the development and maintenance of obstacle flow patterns. Without considering the effect of this pressure he was unable to account for the large pressure observed in an updraft of a newly developed cell on the upstream side of a larger thunderstorm.

At 45 min a relative horizontal high is located along the left edge of the cloud. This pressure may be closely associated with dynamic pressure induced after cloud formation and just upwind of the updraft
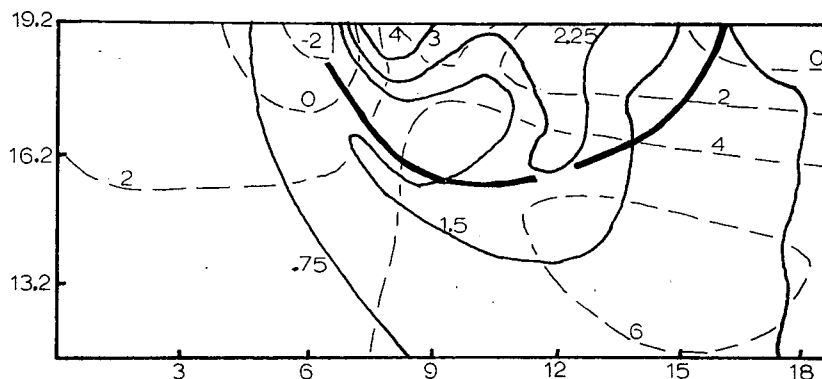

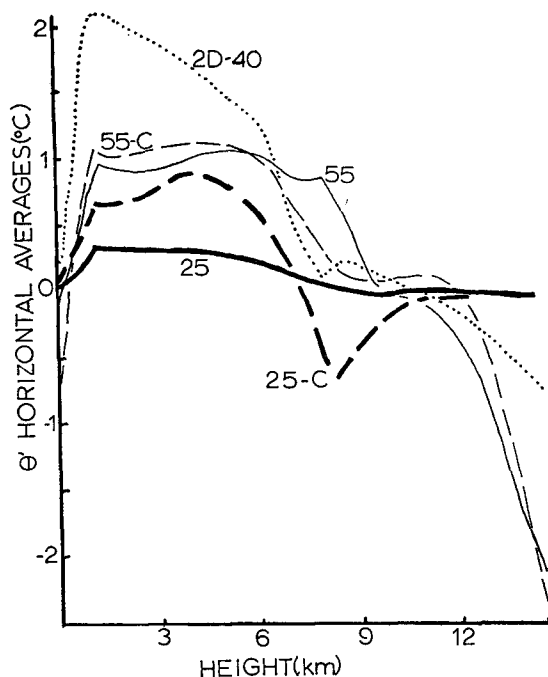FIG. 22. As in Fig. 11 except at 6.9 km and 45 min.

FIG. 23. Horizontal averages for θ' at 25 (thick) and 55 (thin) min. The solid lines are averages for the horizontal planes and the dashed lines for just the central plane portion denoted also by C. The dotted line is for the averages of the two-dimensional simulation (2D) at 40 min.

The changes in atmospheric conditions during the lifetime of a numerically simulated cloud may not only provide a better understanding of one's model, but also provide useful information for those attempting to further understand the importance of cloud-scale effects on larger scale phenomena.

Horizontal averages at 25 and 55 min are given in Figs. 23–26 for the deviations of θ, u and Q_v from their initially specified base states. These averages give some insight into the net changes at a given level in the domain due to the presence of the cloud up to the chosen times. The figures also include horizontal averages for just the central plane.

The θ' averages are mostly positive in the lower half of the domain. These positive averages can be associated with the net release of latent heat. This is evident by integrating (4) in time and space to give

$$\langle \theta' \rangle = \int_0^t \left[\frac{-1}{\bar{\rho}} \frac{\partial \langle \bar{\rho} w \theta \rangle}{\partial z} + \frac{L}{C_p \pi} \langle P2 - P3 - P4 \rangle \right.$$

$$\left. + \left\langle \frac{\partial}{\partial z} \left(K \frac{\partial \theta'}{\partial z} \right) \right\rangle \right] dt, \quad (12)$$

where $\langle \ \rangle$ denotes the horizontal average. In Fig. 24 $\langle \theta' \rangle$ and the second term on the right of (12) representing the average net release of latent heat are

core. Dynamic pressure results from the advective terms on the right-hand side of (2). Thus both dynamic and hydrostatic pressure appear to be associated with upwind blocking of flow in the present model.

High and low centers of horizontal pressure have been indicated with all w horizontal contours. The general tendency is for high centers to be located along the central plane and somewhere to the left of the updraft core center. The low centers are typically to the right of the updraft core, and at 0.9 and 3.9 km they are away from the central plane. This implies a general horizontal acceleration of u across the cloud in the downshear direction by pressure forces. The differences between these marked low and high centers at a given level range from 0.2 to 0.8 mb. These differences vary by a small amount depending on how the pressure constant is chosen since π' is only determined to within an arbitrary constant from (2). Here π' has been assumed to be zero in the upper left corner of the central plane.

e. Some diagnostics

The importance of parameterizing the convective transport of heat, moisture and momentum is well recognized, particularly in the tropics where large-scale circulations are primarily driven by the release of latent heat in cumulus and cumulonimbus clouds.
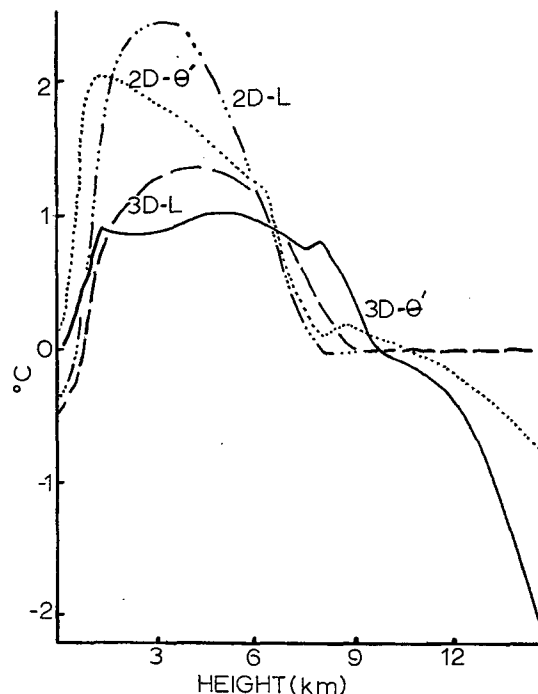

FIG. 24. Horizontal averages of θ' for the three-dimensional simulation (3D) at 55 min and the two-dimensional simulation (2D) at 40 min together with curves (3D-L, and 2D-L, respectively) representing the contribution of the net release of latent heat to those averages.

plotted at 55 min. Both are positive and similar in the lower half of the domain.

In the upper part of the domain where the potential temperature lapse rate is about 10C km^{-1} there is a noticeable drop in $\langle\theta'\rangle$. This appears to be primarily the result of dry adiabatic cooling near the top boundary as very little evaporation occurs in the upper 3 km. Further indication of this is that just below the top boundary the potential temperature can be reduced by upward parcel movement. However, downward moving parcels do not compensate for this cooling as $w=0$ at the top boundary.

The averages for u' in Fig. 25 indicate a distinct decrease in u at mid-levels within the central plane. This would appear to be the result of the upward transfer of horizontal momentum and is consistent with cloud movement to the left. In Fig. 26 the plotted Q_v' averages indicate a notable reduction of moisture in low levels at 55 min. The large central plane averages are probably associated with saturated parcels rising in the cloud and evaporation of cloud water along the cloud edges.

The above observations about horizontally averaged fields are not complete in that the cloud persists beyond 55 min; however, they do indicate some basic adjustments in the environment. Since in this model the domain is closed to outside influences there should be a net increase in potential temperature after cloud dissipation as rain falling out of the system will not evaporate. Therefore, the horizontally averaged distribution of θ' after cloud decay may be somewhat similar to that at 55 min. Some two-dimensional experiments mentioned in the Appendix indicate the plausibility of this conjecture. Also, it should be said
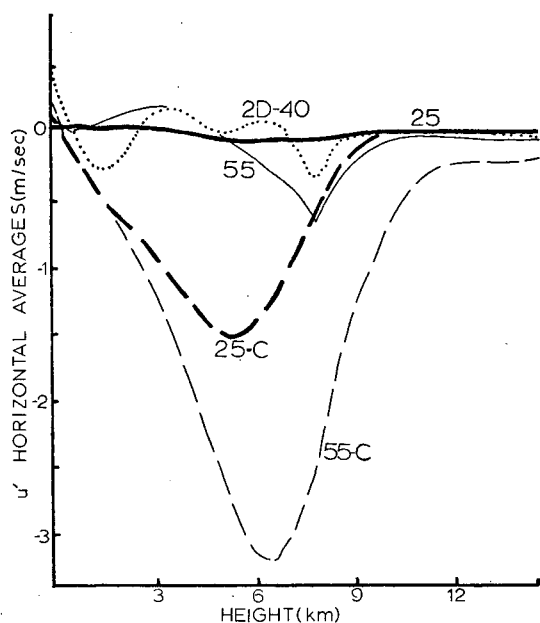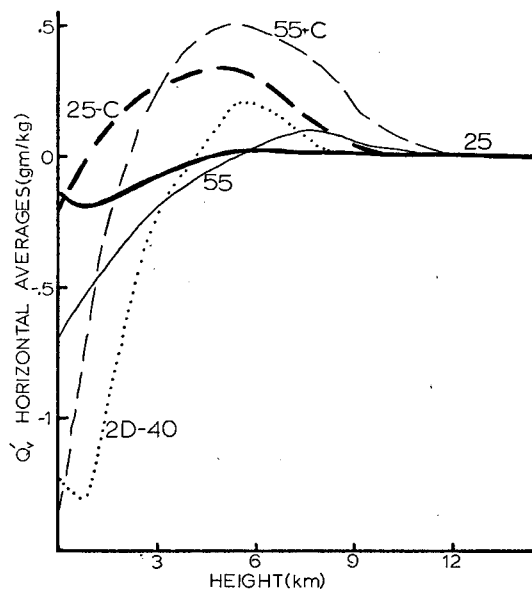

FIG. 26. As in Fig. 23 except for Q_v'.

that the θ and Q_v fields were initially perturbed and the excess temperature and moisture introduced were not included in the base state. In some simulations this might be important to consider, but here the average deviations discussed would not be significantly altered if they were determined from the base state plus the horizontal averages of θ' and Q_v' for the initial impulse.

In concluding this section some comments concerning condensation, evaporation and rainfall are given. The total amount of condensation at 55 min is 1929×10^9 gm with the largest total amount of condensation occurring at 2.7 km. The relative maximum total condensation rates occur from 24 to 25 and from 36 to 37 min, the same periods when the relatively largest maximum w's occur. The total amount of evaporation at 55 min is 597×10^9 gm with the largest amount occurring at 2.1 km. The relatively largest evaporation rates occur before and after the two largest condensation rates, namely from 20 to 21 and from 49 to 50 min. Evaporation always exists 1 km or so above the highest condensation level. The total rainfall at 55 min is 589×10^9 gm with the largest rainfall intensity having occurred at 45 min. The total rainwater content peaks at 40 min. Finally, it should be noted that the amount of water vapor supplied in the initial impulse was 30×10^9 gm, considerably less than the above amounts of condensation, evaporation and rainfall.

5. A two-dimensional counterpart

a. Two-dimensional results

A two-dimensional (2D) slab-symmetric simulation assuming $v=0$ in Eqs. (1)–(10) was made in order

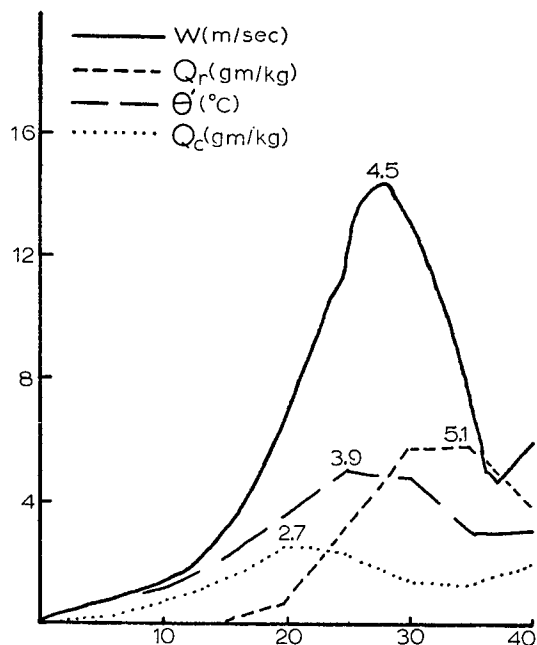FIG. 25. As in Fig. 23 except for u'.

FIG. 27. As in Fig. 2 except for 2D.

to compare results with those for the central plane of the three-dimensional (3D) simulation already described. The initial conditions including grid and domain size for the 2D simulation were exactly the same as those for the 3D central plane. Comments in the numerical section concerning advection to and from the central plane should be noted. Fig. 27 gives a general summary indicating w and Q_r maxima to be about half of those in three dimensions, while those of θ' and Q_c are about the same (see Fig. 2). The

larger w and Q_r in 3D are associated with differences in available moisture supply in low levels and the subsidence rate in the surrounding environment, both reflecting geometric differences. Soong and Ogura (1973) comment on the ratio of the maximum w between slab-symmetric and axisymmetric models in which the horizontal wind is initially zero. The ratio between 2D and 3D is 0.51, close to the 0.53 ratio of Soong and Ogura and between the 0.12 ratio of Murray (1970) and the 0.71 ratio of Wilhelmson (1972). With respect to subsidence, the ratio of the maximum w in the updraft core to the minimum w near the cloud edge taken at their respective peak w times is about 8.5 for 3D and 2.9 for 2D. Similar maxima of θ' which are at nearby vertical levels may indicate parcels rising along similar wet adiabats while similar maxima of Q_c are indicative of the same auto-conversion parameterization.

The maximum 3D velocity occurs 4 min earlier than and several kilometers above that of 2D. The 3D cloud reaches a peak height of 9.3 km $(Q_c+Q_r \geqslant 10^{-5}$ gm gm$^{-1})$ at 25 min while the 2D cloud reaches its peak height of 8.1 km about 5–10 min later. A maximum rainfall intensity in 3D of 157 mm hr^{-1} occurs at about 45 min while a considerably less intensity in 2D of 51 mm hr^{-1} occurs at 40 min. There is in 2D, then, a general lag in the development of a less intense and smaller cloud in comparison to the 3D cloud simulated.

Some 2D results at 35 min are given in Figs. 28–31. Immediately noticeable from the w contour are the two new updraft cells on either side of the downdraft. The left cell is responsible for the upswing in w at 40 min in Fig. 27. The 3D results show little development of new cells in the central plane.
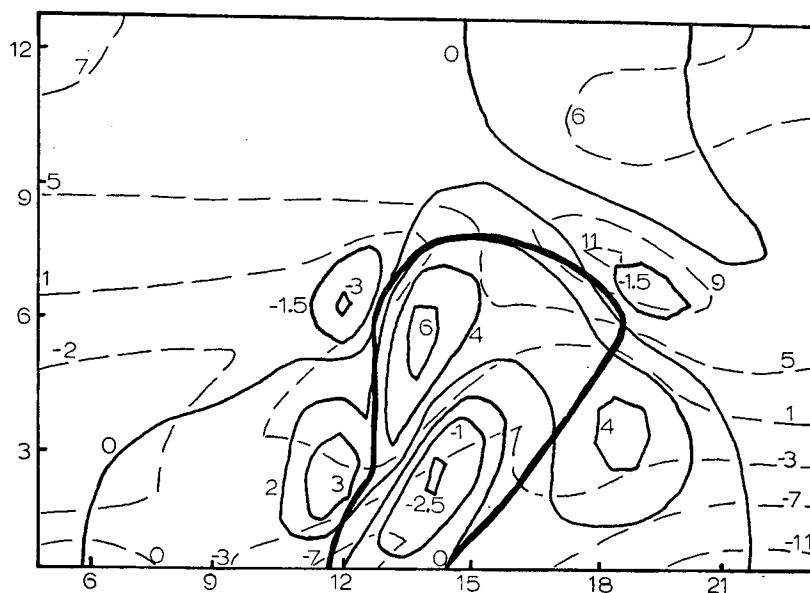

FIG. 28. As in Fig. 3 except for 2D at 35 min.

The pattern of the u contours in Fig. 28 look similar in the middle and upper parts of the cloud to those in the central plane of 3D at 45–55 min, although with a more pronounced slant. In the cloud environment there is a decrease of horizontal wind shear to the cloud left and an increase to the cloud right, also noted for 3D. The lower level pattern differs, however, as the downdraft forms. There are large negative values of up to -12 m sec^{-1} to the right of the downdraft region and values down to about -7 m sec^{-1} in the downdraft region, while in 3D there are values of only about -4 to -5 m sec^{-1} to the right but -12 m sec^{-1} in the downdraft region. The large values to the right of the 2D downdraft appear to be associated with air converging from the right toward the new right updraft already noted. The larger values in the downdraft region of the 3D case would seem to be associated with the stronger downdraft in a more intense cloud.

The 2D pressure deviation field in Fig. 29 indicates a high located at the ground along the right-hand edge of the downdraft. The horizontal pressure force associated with this high opposes right cell inflow in low levels while encouraging outflow to the left in the low part of the downdraft region. In the upper part of the cloud a high located in a similar position to those in the central plane for 3D (see Figs. 4 and 8) existed at 25 min but by 35 min has vanished. This is indicative of the decay of the original updraft. Overall, the π' field indicates that the vertical pressure force opposes cloud growth in all but the lower levels as in 3D. Schlesinger (1973b) has also noted for his prototype simulation in two dimensions with wind shear that the vertical pressure gradient force tends to oppose the thermal buoyancy force in the middle

and upper cloud levels. Similar comments have been made by Soong and Ogura (1973) for slab-symmetric and axisymmetric models.

The Q_r and Q_c fields are given in Fig. 30. The raindrops have been carried to the right of the updraft where they are falling to the ground as in 3D. Condensation in the new left updraft is seen to be important to its growth. The new right updraft appears to be primarily supported by the upward diversion of air converging from the right, not by the release of latent heat as little condensed vapor exists in its core. The relative wind vectors in Fig. 31 indicate such flow. It is somewhat difficult, however, to talk about the cloud speed at 35 min needed in determining the relative flow pattern for Fig. 31 in view of the decay of the original cloud and the formation of new updraft cells. The cloud speed determined by following the horizontal movement of the maximum w in the original updraft indicates the cloud speed has changed from -4 m sec^{-1} at 10 min to zero at 30 and 35 min.

In Figs. 23, 25 and 26 the horizontal averages for 2D at 40 min are given. The θ' average curve in Fig. 23 indicates an increase in potential temperature over the depth of the cloud. This increase is larger than for any of the 3D curves between the ground and 6 km. In Fig. 24 it is seen that the net release of latent heat is primarily responsible for this increase over most of the cloud depth. Near the ground the argument for advective cooling of upper air given in Section 5e (also applicable here) may apply in reverse. This would explain the large $\langle \theta' \rangle$ values where the net release of latent heat is small. Further, this warming would tend to be greater in 2D because of geometric constraints on subsidence induced by the cloud.
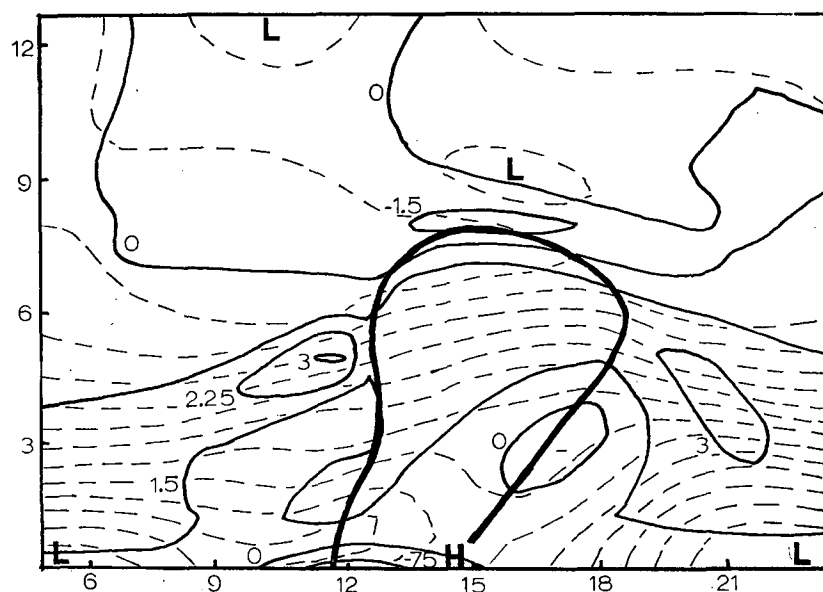

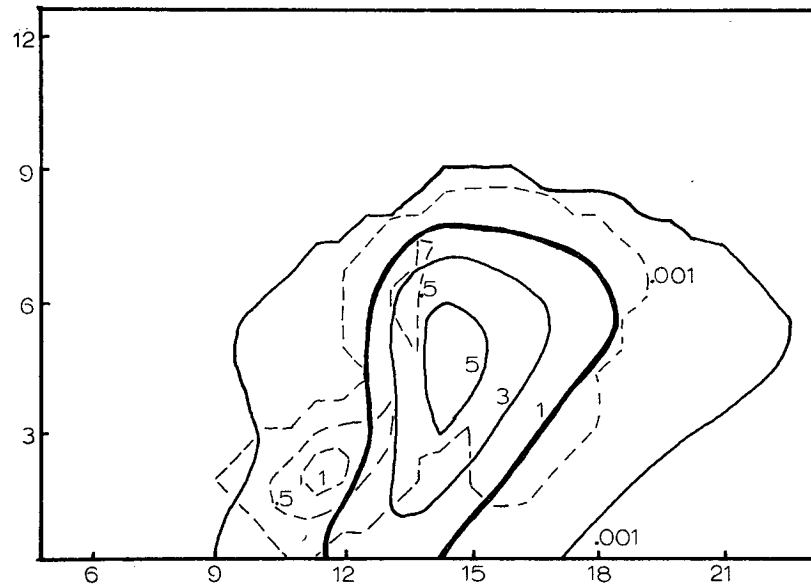FIG. 29. As in Fig. 4 except for 2D at 35 min.

FIG. 30. As in Fig. 5 except for 2D at 35 min.

The u' and Q_v' average curves are included in Figs. 25 and 26 for completeness. The u' averages in Fig. 25 are small in comparison to those of the central plane for 3D. The Q_v' averages in Fig. 26 indicate a decrease in Q_v' in the lower levels over a greater depth than in 3D at 55 min.

b. Other two-dimensional experiments

Several two-dimensional experiments were run with slight modifications to the 2D model of Section 5a. In the first the environmental wind was set to zero.

The results indicate a maximum vertical velocity several minutes earlier and 5 m sec⁻¹ greater than for the original 2D simulation. The cloud reached a height of 9.9 km at 30 min, about 1.8 km higher than the original 2D cloud, and the maximum rain intensity was also greater. Thus, the effect of the initially specified 2D wind shear was a decrease in cloud intensity and height. Results from the Thunderstorm Project (Byers and Braham, 1949) suggest such an effect of shear on isolated thunderstorms with cores only a few kilometers in diameter.
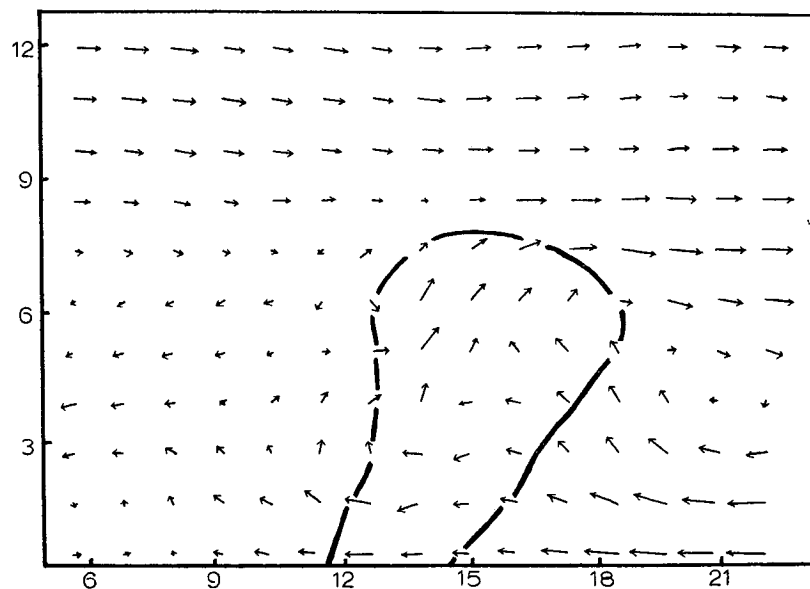
In the second experiment raindrops (Q_r) were al-

FIG. 31. Relative wind vectors for 2D at 35 min. The magnitude
of the largest vector is 12.2 m sec⁻¹.

lowed to evaporate instantaneously until the air became saturated if there were not sufficient cloud droplets (Q_c) for this purpose. Evaporation of all water up to saturation has been used recently in the simulations of Takeda (1971) and Schlesinger (1973a). The maximum velocities occur at the same time and differ by only 0.1 m sec^{-1}. The rain, however, reaches the ground 5–10 min later than in the original 2D. At 35 and 40 min the total evaporation in the domain was about twice as great. The potential temperature was about 3C lower below the cloud, the width of the cloud was less, and the maximum downdraft in the rain area was almost twice as intense due to additional evaporation. These results indicate the quantitative sensitivity of the model to the method of handling evaporation.

6. Summary and conclusions

a. Results of this paper

A comparison of cloud growth and decay in an initially sheared environment for a two- and three-dimensional simulation reveals some basic differences. The three-dimensional cloud (3D) grows about 1 km higher and has w and Q_r maxima about double those of the two-dimensional (2D) cloud. It also develops faster, lasts longer, and travels to the left farther and faster than the 2D cloud. This is indicative of the differences in geometry which, in turn, are related to low-level moisture supply for cloud growth and subsidence in the cloud environment. The ratio of the maximum w to the minimum w or subsidence near the cloud edge is about 8.5 for the 3D case and 2.9 for the 2D case, these ratios being calculated when the maximum w occurred in each case. The maximum rainfall intensity in 3D is about three times that of 2D. A new cloud develops to the left of the 2D cloud as it dies at 40 min but none develops on either side of the 3D cloud by 55 min as it continues to decay.

There are also several similarities that stand out. During the development stage both clouds move with the initial horizontal wind in the lower 2 km. In both cases the updraft cores never leans upshear (to the left). Thus, rain carried aloft by the updraft falls predominantly to the right of the updraft core, cutting off at low levels the core's primary supply of warm and moist air. Finally, the vertical pressure force generally opposes cloud growth at all times.

Looking at the horizontal features of the 3D simulation reveals that the updraft core is fed from all directions by moist and warm low-level air as the cloud develops. As time passes and rain begins to fall, the lower level center of the updraft core is shifted away from the central plane as the downdraft forms in the rain region. The core then rises up and over the downdraft, back to the central plane. In the upper part of the cloud relative diverging air flows out from the cloud and then moves in the direction of the general relative wind at the same height.

At middle levels the relative air velocity vectors appear to indicate passage of air both around and into the cloud. Wind features reminiscent of flow about a cylinder are indicated by a low u center located on the central axis and upshear of the cloud and an increase in u along the sides of the cloud at 25 and 45 min. At 25 min the excess hydrostatic or buoyancy pressure appears to be most important in decelerating upshear flow, while at 45 min the dynamic pressure induced after cloud formation has gained in importance. Thus, both dynamic and hydrostatic pressure appear to be associated with upwind blocking of flow in the present model.

Horizontal averages of potential temperature, horizontal velocity, and vapor mixing ratio were computed in light of interest in the net effects of a cloud's growth and decay on its environment. One difference between the two- and three-dimensional simulations was the greater average heating over the cloud depth in the 2D simulation. Upon breaking this average down in contributing parts the increase appears to be primarily associated with an increased net average release of latent heat.

b. Three-dimensional modeling of clouds

In the Introduction the present study was characterized as an initial effort to investigate the importance of using three dimensions for modeling precipitating deep convection in an environment sheared in one direction. The differences between the reported two- and three-dimensional simulations help emphasize the importance of three-dimensional modeling in understanding observed storm features such as air flow around a storm. The development and use of three-dimensional models does not come, however, without additional considerations and costs, both for carrying out the simulations and for understanding the results.

Large and fast computers are capable of solving many three-dimensional problems. However, they do have speed, memory and auxiliary storage limits. The modeler is required to know the limits of the computer he is using and develop his model weighing these limitations with his objectives. He may choose a numerical method that will help minimize the needed transfer of data between main memory and auxiliary storage. He may limit his domain size or increase his grid interval size to hold down data storage requirements. The modeler may decide that the grid be moved with the cloud as it changes direction or speed. Rerunning the simulation with the initial horizontal wind field adjusted by a constant in order to attempt to keep the cloud in or near the center of the domain when nonperiodic lateral boundaries are used may no longer be feasible from the standpoint of the high computer and time costs involved.

In order to understand the dynamics simulated the modeler must decide on effective ways to look at his data. Here he is in a similar position to the observa-

tionalist who has collected his data from radar, aircraft and other sources, although, in numerical modeling, there usually is considerably more data available. Time requirements for proper analysis of the three-dimensional features simulated by the modeler may be considerably larger than those for analysis of two-dimensional simulations.

These comments are made not to discourage three-dimensional modeling, but rather to emphasize that careful consideration of objectives be given when one is modeling storms as some of these objectives may be accomplished with or in conjunction with two-dimensional models. Such consideration has been emphasized by others including Orville and Sloan (1970).

c. Model improvements

Several possible improvements to the present model are suggested. These are based on a general desire to simulate and better understand cloud growth, decay and possible regeneration. One requirement that would appear to be necessary is the ability to numerically integrate the model equations over an extended time period of time, perhaps up to 3 hr. Numerical difficulties concerning gravity waves were encountered in the present simulations. There is some indication from two-dimensional experiments given in the Appendix that a reduction in Δt for the scheme used may be sufficient to prevent large gravity-wave amplification. An alternative approach would be the adoption or development of a different scheme, perhaps a scheme that is second order in space and time. Among other effects of such a choice may be increased computer storage requirements and the need to adjust water fields when negative water occurs due to advection.

Another possible improvement for long-term integrations might be the adoption of different lateral boundary conditions. This decision may be crucial to model results. Continued cloud growth and regeneration depend on a sufficient and properly located moisture supply and on the environmental conditions into which the storm moves or regenerates itself. The lateral boundary conditions, in particular, represent a bridge between the storm scale and higher scales of motion that may provide this moisture supply and appropriate environmental conditions. Takeda (1971) indicated a lack of success in his attempts to model air flow across the lateral boundaries due to cloud disturbances in a two-dimensional domain. The need for a better understanding of this bridge is underscored when one considers moving one's grid with the cloud. In some way one needs to fill in variable values at the new grid points created by the move and, in particular, for the velocity field without violating the mass continuity equation.

A final suggestion would be the release and tracing of parcels from time to time. A record of the forces acting on these parcels and of their movement might be helpful in understanding the dynamics of a storm, including its movement and momentum transports.

APPENDIX

Amplifying Internal Gravity Waves and Numerical Instability

A von Neumann stability analysis of the linearized difference equations representing gravity waves in a dry atmosphere is presented here. The linearized gravity wave equations similar to those given by Ogura and Charney (1962) are

$$\left.\begin{array}{c} \hat{u}_t = -p_x' \\ \hat{w}_t = -p_z' + \Theta g \\ p'_{xx} + p'_{zz} = g\Theta_z \\ \Theta_t = -\hat{w}S \end{array}\right\}, \qquad (A1)$$

where $\hat{u} = \bar{\rho}u$, $\hat{w} = \bar{\rho}w$, $\Theta = \rho\theta'/\bar{\theta}$, $S = \partial \ln\bar{\theta}/\partial z$ and $p = \bar{p} + p'$; and $\bar{\rho}$, $\bar{\theta}$, θ', $\bar{p}$ are as defined in this paper but for a dry atmosphere. Difference solutions for u, w, Θ and p' of the form

$$f_{j,k}^n = \tilde{f}^n e^{i(lj\Delta x + mk\Delta z)} \qquad (A2)$$

are assumed for any wavenumbers l and m where $x = j\Delta x$, $z = k\Delta z$ and $t = n\Delta t$. When the equations in (A1) are expressed using forward time and centered space differences over the staggared grid of Fig. 1 and when the assumed difference solutions are substituted into these equations, the result is

$$\left.\begin{array}{c} \tilde{u}^{n+1} = \tilde{u}^n - A\tilde{p}^n \\ \tilde{w}^{n+1} = \tilde{w}^n - B\tilde{p}^n + C\tilde{\Theta}^n \\ \tilde{\Theta}^{n+1} = \tilde{\Theta}^n - D\tilde{w}^n \\ \tilde{p}^{n+1} = E\tilde{\Theta}^{n+1} = E\tilde{\Theta}^n - E \cdot D\tilde{w}^n \end{array}\right\}, \qquad (A3)$$

where

$$A = 2i(\Delta t/\Delta x)\sin(l\Delta x/2),$$

$$B = 2i(\Delta t/\Delta z)\sin(m\Delta z/2),$$

$$C = g\Delta t\,\cos(m\Delta z/2),$$

$$D = S\Delta t\,\cos(m\Delta z/2),$$

$$E = \frac{-i(g/\Delta z)\sin(m\Delta z)}{(2/\Delta x)^2\sin^2(l\Delta x/2) + (2/\Delta z)^2\sin^2(m\Delta z/2)}.$$

Writing (A3) in matrix form gives

$$\mathbf{X}^{n+1} = \mathbf{V}\mathbf{X}^n, \qquad (A4)$$

where

$$X^n = [\tilde{u}^n, \tilde{w}^n, \tilde{\Theta}^n, \tilde{p}^n]^T,$$

$$V = \begin{bmatrix} 1 & 0 & 0 & -A \\ 0 & 1 & C & -B \\ 0 & -D & 1 & 0 \\ 0 & -DE & E & 0 \end{bmatrix}.$$

The eigenvalues λ_i of the amplification matrix V are given by

$$\lambda(1-\lambda)[\lambda^2 - 2\lambda + (1 + DC - BDE)] = 0, \qquad (A5)$$

which has roots

$$\left. \begin{array}{l} \lambda_1 = 1, \quad \lambda_2 = 0 \\ \lambda_{3,4} = 1 \pm (BDE - DC)^{\frac{1}{2}} \end{array} \right\}.$$

For $S > 0$ (stable atmosphere)

$$BDE - DC = \frac{-gS[a\Delta t \cos(m\Delta z/2]^2}{a^2 + b^2} < 0,$$

where

$$\left. \begin{array}{l} a = \sin(l\Delta x/2)/\Delta x \\ b = \sin(m\Delta z/2)/\Delta z \end{array} \right\}.$$

Thus

$$|\lambda|^2 = 1 + \frac{gS[a\Delta t \cos(m\Delta z/\Delta 2)]^2}{a^2 + b^2} \geq 1, \qquad (A6)$$

indicating the instability associated with the numerical scheme employed for representing linearized gravity wave motion. Forward time and centered space differencing applied to (A1) in vorticity form also leads to similar instability.

Several comments on (A6) are appropriate. First, for a given Δt the larger the atmospheric stability S the larger the amplification. In the reported simulation the numerical amplification of gravity waves is encouraged by the stability of the atmosphere in the upper part of the domain.

Second, representing (A6) as

$$|\lambda|^2 = 1 + (\Delta t)^2 G_{l,m}, \qquad (A7)$$

TABLE 1. Brief descriptions of several two-dimensional simulations illustrating the relationship between the safety factor (i.e., choice of Δt), the amplification of gravity waves, and the effect of eddy diffusion on the maximum updraft.

Run	Safety factor	Explicit eddy diffusion	Maximum w (m sec⁻¹) and time (min)	Noticeable amplification time (min)
2D	0.9	yes	14.37–28	40
2D–6	0.5	yes	13.92–28	55
2D–12	0.4	yes	13.66–28	65
2D–9	0.5	no	15.33–28	55
2D–13	0.4	no	15.06–27	65
2D–11	0.2	no	14.31–27	none to 90 min

for any given wavenumbers l and m, one can show that as Δt approaches zero the amplification factor becomes less. To span a $2\Delta t$ time interval, a reduction in Δt to $\Delta t/2$ requires twice the number of steps, with an associated amplification of

$$|\lambda|^4 = [1 + (\Delta t/2)^2 G_{l,m}]^2.$$

Provided that Δt is sufficiently small such that

$$(\Delta t)^2 G_{l,m} < 8,$$

the amplification over the $2\Delta t$ time span will be less. Several two-dimensional experiments similar to that discussed in Section 5 but using smaller safety factors for Eg. (11) indicate delays and reduction in amplification (see Table 1).

The numerical problem with reducing Δt when using the forward time and upstream advective technique is the associated increase of implicit diffusion. This is also illustrated in Table 1 along with the effect of ignoring the explicit diffusion in some cases, i.e., $F = 0$. In comparing experiments with the same safety factor it should be noted that the choice of Δt using (11) may still be different at any given time but that in these experiments this difference should not affect the general comparative outcome. Also, it should be noted that the basic dynamical features are similar until the cloud decays or gravity wave amplification becomes noticeable.

One possible conclusion from these experiments is that when the effect of turbulence or eddy diffusion is not of major interest a reduction in Δt to control gravity wave amplification may be justified. This will, however, have some quantitative effects.

REFERENCES

Asai, T., 1967: An example of cumulus updraft as revealed by rawinsonde observation. J. Meteor. Soc. Japan, 45, 493–495.

Barnes, S. L., 1970: Some aspects of a severe, right-moving thunderstorm deduced from mesonetwork rawinsonde observations. J. Atmos. Sci., 27, 634–648.

Byers, H. R., and R. R. Braham, 1949: The Thunderstorm. Washington, D. C., Govt. Printing Office, 67–68.

Deardorff, J. W., 1970: A numerical study of three-dimensional turbulent channel flow at large Reynolds numbers. J. Fluid Mech., 41, 453–480.

——, 1972: Numerical investigation of neutral and unstable planetary boundary layers. J. Atmos. Sci., 29, 91–115.

Fankhauser, J. C., 1971: Thunderstorm-environment interactions determined from aircraft and radar observations. Mon. Wea. Rev., 99, 171–192.

Foote, G. B., and J. C. Fankhauser, 1973: Airflow and moisture budget beneath a northeast Colorado hailstorm. J. Appl. Meteor., 12, 1330–1353.

Hane, C. E., 1973: The squall line thunderstorm: Numerical experimentation. J. Atmos. Sci., 30, 1672–1690.

Jessup, E. A., 1972: Interpretations of chaff trajectories near a severe thunderstorm. Mon. Wea. Rev., 100, 653–661.

Murray, F. W., 1970: Numerical models of a tropical cumulus cloud with bilateral and axial symmetry. Mon. Wea. Rev., 98, 14–28.

Newton, C. W., 1966: Circulations in large sheared cumulonimbus. Tellus, 18, 669–712.

——, 1967: Severe convective storms. *Advances in Geophysics*, Vol. 12, New York, Academic Press, 257–308.

——, and H. R. Newton, 1959: Dynamical interactions between large convective clouds and environment with vertical shear. *J. Meteor.*, **16**, 483–496.

Ogura, Y., 1963: The evolution of a moist convective element in a shallow, conditionally unstable atmosphere: A numerical calculation. *J. Atmos. Sci.*, **20**, 407–424.

——, and J. C. Charney, 1962: A numerical model of thermal convection in the atmosphere. *Proc. Intern. Symp. Numerical Weather Prediction, Tokyo*, 7–13 November 1960, 431–451.

Orville, D. O., and L. J. Sloan, 1970: A numerical simulation of the life history of a rainstorm. *J. Atmos. Sci.*, **27**, 1148–1159.

Roberts, L., and B. Wessler, 1970: Computer network development to achieve resonance sharing. *Proc. AFIPS Spring Joint Computer Conf.* No. 36, Washington, D. C., Spartan, 543–549.

Schlesinger, R. E., 1973a: A numerical model of deep moist convection: Part I. Comparative experiments for variable ambient moisture and windshear. *J. Atmos. Sci.*, **30**, 835–856.

——, 1973b: A numerical model of deep moist convection: Part II. A prototype experiment and variations upon it. *J. Atmos. Sci.*, **30**, 1374–1391.

Sher, M. S., 1973: Experience in networking—A case study. *EDUCOM, Bull. Interuniversity Commun. Conn.*, **8**, 8–13.

Soong, S., and Y. Ogura, 1973: A comparison between axisymmetric and slab-symmetric cumulus cloud models. *J. Atmos. Sci.*, **30**, 879–893.

Steiner, J. T., 1973: A three-dimensional model of cumulus cloud development. *J. Atmos. Sci.*, **30**, 414–435.

Takeda, T., 1971: Numerical simulation of a precipitating convective cloud: The formation of a long-lasting cloud. *J. Atmos. Sci.*, **28**, 350–376.

Wilhelmson, R., 1972: The numerical simulation of a thunderstorm cell in two- and three-dimensions. Ph.D. thesis, University of Illinois.

——, and Y. Ogura, 1972: The pressure perturbation and numerical modeling of a cloud. *J. Atmos. Sci.*, **29**, 1295–1307.

Williams, G. P., 1969: Numerical integration of the three-dimensional Navier-Stokes equations for incompressible flow. *J. Fluid Mech.*, **37**, 727–750.